A Two-Layer Turbulence-based Model to Predict Suspended Sediment Concentration in Flows with Aquatic Vegetation

Chien-Yung Tseng¹, Rafael O. Tinoco¹

¹Department of Civil and Environmental Engineering, University of Illinois at Urbana-Champaign, Urbana, IL, USA

Key Points:

12

- We present a two-layer, turbulence-based model to predict suspended sediment concentration in flows with emergent vegetation.
- We include coherent structures generated by stem-bed-flow interactions to calculate near-bed turbulent kinetic energy.
- We derive models for effective boundary layer thickness and effective bed shear velocity to predict suspended sediment concentration.

Corresponding author: C.-Y. Tseng, cytseng2@illinois.edu

Abstract

14

15

16

18

19

20

21

22

23

25

26

27

28

29

30

31

33

34

35

37

41

42

43

44

45

49

50

51

52

53

57

58

61

62

Traditional bed shear stress-based models (e.g., Rouse model) derived from the classic parabolic profile of eddy viscosity in open-channel flows fail to accurately predict suspended sediment concentration (SSC) in flows with aquatic vegetation. We developed a two-layer, turbulence-based model to predict SSC profiles in emergent vegetated flows. Turbulence generated from vegetation, bed, and coherent structures caused by stem-bed-flow interaction are considered into the near-bed turbulent kinetic energy (TKE) to calculate the effective bed shear velocity, u_{beff}^* . The model, validated by experimental data, further showed that the thickness height of the near-bed layer (effective bottom boundary layer), H_b , varies with flow velocity and canopy density. Two additional models are provided to estimate H_b and u_{beff}^* . The model is expected to provide critical information to future studies on sediment transport, landscape evolution, and water quality management in vegetated streams, wetlands, and estuaries.

Plain Language Summary

Aquatic vegetation serves important roles in wetlands, estuaries, riverine, and coastal areas. It provides shelter for living organisms, protects coastal and riverbank regions from waves, currents, and floods, and makes a contribution to the global carbon circulation. However, under various scenarios of environmental change, the presence of aquatic vegetation continuously decreased in these areas during recent decades. To improve restoration efforts and protect vegetation habitats, understanding vegetation-sediment dynamics is paramount and will lead to more accurate models of landscape evolution and water quality management. Traditional suspended sediment models widely applied in openchannel flows do not work in regions with aquatic plants. We propose a modified model to predict suspended sediment concentration in vegetated flows, validated with experimental data. The new model showed that near-bed turbulence generated by bed-vegetation-flow interaction is as important as the bed- and vegetation-generated turbulence considered separately. The model is expected to provide critical information for future studies on sediment transport, landscape evolution, and water quality management in vegetated streams, wetlands, and estuaries.

1 Introduction

Aquatic vegetation serves multiple roles in maintaining the functionalities of the ecosystem in wetlands, estuaries, riverine, and coastal areas (Micheli & Kirchner, 2002; Danielsen et al., 2005; Dalrymple & Choi, 2007; Kakeh et al., 2015). In addition to local influences, vegetation in these ecosystems also have global impacts. For example, coastal plants such as mangroves, salt marshes, and seagrasses provide an essential portion of carbon storage by global sequestration (Bouillon et al., 2008; Duarte et al., 2010; Kennedy et al., 2010). However, according to recent studies, a significant amount of aquatic vegetation has been lost continuously during past decades (Marani et al., 2011; Mcleod et al., 2011). To improve restoration efforts under multi-scale environmental changes (such as sea level rise, landscape evolution, and anthropogenic pollution), it is necessary to improve understanding of the underlying mechanisms of sediment transport (Syvitski et al., 2009; Paola et al., 2011; Weston, 2014). In particular, we need to better understand how water, sediment, and vegetation interact in regions with vegetation, to accurately predict suspended sediment concentration (SSC), the evolution of vegetated landscapes, and water quality (e.g., sediment oxygen demand; O'Connor & Hondzo, 2008; Waterman et al., 2016).

Sediment transport has long been an important issue for hydraulic and environmental engineers, which has been widely studied in open-channels (e.g., Garcia, 2008, and references therein). In the past, sediment transport and resuspension models relied on measurements of bed shear stress (e.g., Meyer-Peter & Muller, 1948; Yalin, 1963; En-

gelund & Fredsoe, 1976; Parker, 1979; van Rijn, 1984; Nino & Garcia, 1998). However, studies have shown that bed shear stress models do not work in regions with vegetation (Yager & Schmeeckle, 2013; Tinoco & Coco, 2014). Those models do not account for the turbulence generated by vegetation (Nepf, 2012), which has been recognized as a prominent feature in natural flow environments that drives sediment resuspension (Sumer et al., 2003; Diplas et al., 2008). Through laboratory experiments, Tinoco and Coco (2016); Yang et al. (2016) have demonstrated how near-bed vegetation-generated turbulence affects the incipient motion of sediment in vegetated flows. Yang and Nepf (2018) proposed a turbulence-based bed-load transport model based on the relation between turbulence-induced lift force and turbulent kinetic energy (TKE), similar to the non-vegetated case discussed by Nino and Garcia (1996). Their model showed a good agreement with experimental data when including both TKE components from vegetative turbulence and bed-shear turbulence.

To construct a more accurate model for predicting SSC, we must consider the local flux of sediment entrained from the bed by near-bed coherent structures, generated by stem-bed-flow interaction (e.g., horseshoe vortex). Previous studies have revealed that these coherent structures can significantly alter the near-bed stress locally in front of cylinders (Schanderl, Jenssen, & Manhart, 2017; Schanderl, Jenssen, Strobl, & Manhart, 2017), resulting in large differences between the time-averaged and instantaneous turbulent quantities (Apsilidis et al., 2015). These fluctuating coherent structures can cause non-negligible contributions to sediment resuspension (Cheng et al., 2018; Li et al., 2018). In response to the above effects, we propose a new framework considering all the turbulence components from 1) vegetation, 2) bed shear, and 3) fluctuating coherent structures, into near-bed TKE calculation for modeling SSC in flows through emergent vegetation. The new turbulence-based SSC model is based on a two-layer effective turbulent stress profile, and accurately predicts SSC measured experimentally.

2 Two-Layer SSC Model

Starting from a traditional approach that considers sediment particles as continuous diffusive scalars, based on equilibrium of suspended sediment without reacting with the fluid, turbulence stress is balanced with sediment's settling as:

$$-D_t \frac{\partial C}{\partial z} - w_s C = 0 \tag{1}$$

where C is the time-averaged SSC, w_s is the sediment settling velocity, and D_t is the flow eddy diffusivity in the vertical direction. D_t is usually equated with the vertical flow eddy viscosity, ν_t , assuming the turbulent Schmidt number, $Sc_t = \nu_t/D_t = 1$, according to Reynolds analogy of eddy mixing. By solving the above differential equation, we can obtain the general form of the SSC profile

$$C(z) = C_b e^{-w_s \int_b^z \frac{1}{\nu_t} dz}$$
 (2)

where C_b is the time-averaged SSC at a reference z-location, b, near the bed. Rouse profile of SSC (Rouse, 1937) has been widely applied in open-channel flows based on a parabolic profile of eddy viscosity, ν_t , as:

$$\nu_t(z) = \kappa u_b^* z \left(1 - \frac{z}{H} \right) \tag{3}$$

where u_b^* is the bed shear velocity and κ is the von Karman constant = 0.41. Replacing Equation 3 into Equation 2, the Rouse profile of SSC can be obtained as:

$$C(z) = C_b \left[\frac{(H-z)/z}{(H-b)/b} \right]^{Z_R} \tag{4}$$

where Z_R is the Rouse number

$$Z_R = \frac{w_s}{\kappa u_b^*} \tag{5}$$

However, in vegetated flows the profile of ν_t is no longer parabolic (Defina & Bixio, 2005), thus Rouse profile cannot be used to accurately predict SSC (Lopez & Garcia, 1998).

According to the turbulent-viscosity hypothesis, ν_t can be obtained by the ratio between the turbulent stress, τ_t , and the mean flow velocity gradient, dU/dz,

$$\nu_t = \frac{\tau_t}{\rho dU/dz} \tag{6}$$

which has been proved valid for simple shear flows (e.g., open channel flows). However, in canopy flows, counter-gradient momentum transport is generally observed close to the bed (Shaw, 1977) due to stem-bed-flow interaction, which could modify the turbulentviscosity hypothesis in the near-bed region (Raupach & Thom, 1981). Hence, we introduce a new, more effective approximation for this near-bed region. Above the near-bed region, Equation 6 still holds and suggests that profiles of mean flow velocity and turbulent stress are key to derive ν_t in vegetated channels. Previous studies have shown a characteristic constant velocity profile above a certain distance from the bed in emergent vegetated flows (Nepf & Vivoni, 2000; D. Liu et al., 2008; Stoesser et al., 2010). Yang et al. (2015) proposed a two-layer linear stress model to predict bed shear stress and the velocity profile in vegetated flows under smooth bed environments. Etminan et al. (2018) further provided a balance argument between TKE production and TKE dissipation rate to precisely estimate the thickness of the viscous layer. However, most of the bottom boundaries in natural water environments are hydraulically rough, where roughness elements (e.g., sediment particles) penetrate through the viscous layer. When $k_s/\delta_{\nu} > 1$, where k_s is the bottom roughness height, and δ_{ν} is the height of viscous layer, viscous layer becomes relatively small and thus negligible. Also, varying bottom roughness can further increase the boundary layer thickness (Schultz & Flack, 2007; Hanmaiahgari et al., 2017).

To account for the bottom roughness effect, we propose a modified two-layer SSC model based on an effective turbulent stress profile for flows with emergent vegetation. In the region close to the bed but above the viscous layer, turbulence generated from both the bed and the vegetation is dominant, which causes counter-gradient momentum transport due to interacting stem-bed-flow coherent structures. To account for such complex interactions, we approximated the turbulent stress profile as an effective linear-stress profile, following Yang et al. (2015), and included the local flux of sediment entrained from the bed due to fluctuating near-bed coherent structures into the near-bed TKE calculation to update the linear turbulent stress (see details in Section 4.4). This region is so called the linear-stress layer or the effective bottom boundary layer. Above the linear-stress layer, the velocity profile reaches a constant value, and the turbulent stress in this region also approaches a constant ($\tau_t = \rho \overline{u'w'} \approx const.$). This region is called the constant velocity layer or the constant stress layer. In this layer, turbulence generated from the bed can be ignored, and sediment suspension is mainly supported by the stem-generated turbulence

By setting H_b as the thickness height of the effective bottom boundary layer, the effective turbulent stress can be expressed as

$$\tau_{eff} = \begin{cases} \rho u_{b\,eff}^*^2 (1 - z/H) &, \quad k_s \le z \le H_b \\ \approx const. &, \quad z > H_b \end{cases}$$
 (7)

where H is the water depth, and u^*_{beff} is the effective bed shear velocity, derived from the total near-bed turbulent stress, which considers turbulence generated from the bed shear stress, vegetation, and the coherent structures. u^*_{beff} is different from the bed shear velocity, u^*_b , in Equation 3, which was derived directly from the bed-shear stress or bed-shear turbulence. More details are described in Section 4.4. Since log-law is assumed valid for the effective velocity profile in the linear stress layer, the effective mean flow velocity gradient can be estimated as

$$\frac{dU_{eff}}{dz} = \begin{cases}
\frac{u_{b\,eff}^*}{\kappa z} &, & k_s \le z \le H_b \\
\approx 0 &, & z > H_b
\end{cases}$$
(8)

Replacing Equation 7 and Equation 8 into Equation 6, the reciprocal of the effective eddy viscosity, ν_{eff} , of the two-layer model can be obtained

$$\frac{1}{\nu_{eff}} = \begin{cases}
\frac{1}{\kappa u_{b\,eff}^* z(1-z/H)}, & k_s \le z \le H_b \\
\approx 0, & z > H_b
\end{cases}$$
(9)

Finally, by further replacing Equation 9 into Equation 2 and solving the integral of $1/\nu_{eff}$, we can obtain the final form of the two-layer model for SSC

$$C(z) = \begin{cases} C_b \left[\frac{(H-z)/z}{(H-b)/b} \right]^{Z_R} &, \quad k_s \le z \le H_b \\ C_b \left[\frac{(H-H_b)/H_b}{(H-b)/b} \right]^{Z_R} &, \quad z > H_b \end{cases}$$
(10)

with an updated Rouse number, $Z_R = w_s/(\kappa u_{beff}^*)$. In the above model, there are two critical parameters that need to be determined: the thickness height of the bottom boundary layer, H_b , and the effective bed shear velocity, u_{beff}^* . We developed two additional models to estimate these parameters in Section 4.3 and Section 4.4, respectively.

3 Methods

3.1 Experimental Setup

The experiment was conducted in an Odell-Kovasznay type recirculating flume (Odell & Kovasznay, 1971, Figure 1(a)), with a straight test section 2 m long, 0.15 m wide, and 0.6 m deep. A vertical axis disk-pump with uniformly distributed disks drives the flow to produce a uniform velocity profile with minimal vertical disturbance. As water continues to recirculate in an essentially infinite loop, the design guarantees full development of the boundary layer and turbulence features in the flume, which ensures applicability of Equation 1 with an assumption that the sediment profile reached equilibrium and fully developed with the flow. The disk rotational frequency, ω , is set by the frequency, f, of an inverter as ω (rpm) = 6.6f (Hz).

High-stiffness aquatic vegetation such as $Sagittaria\ sagittifolia\ and\ Sparganium\ erectum$ are mimicked by an array of rigid acrylic cylinders with diameter $d=0.64\ cm$. The water depth, H, is set as $10\ cm$. The length of vegetation array is $156.2\ cm\ (246\ d)$, and the leading edge is $20.3\ cm\ (32\ d)$ downstream from the beginning of the straight test section. A $7.6\ cm\ (12\ d)$ gap was left within the array from $135.3\ cm$ to $142.9\ cm\ (213\ d)$ to $225\ d$) from the beginning of the array for Particle Image Velocimetry (PIV) and SSC measurement. A staggered configuration was used with two array densities to cover from sparse to dense conditions, $ah=\{0.1\ -0.5\}\ (Nepf,\ 2012)$. The detailed array configuration is shown in Figure 1(b).

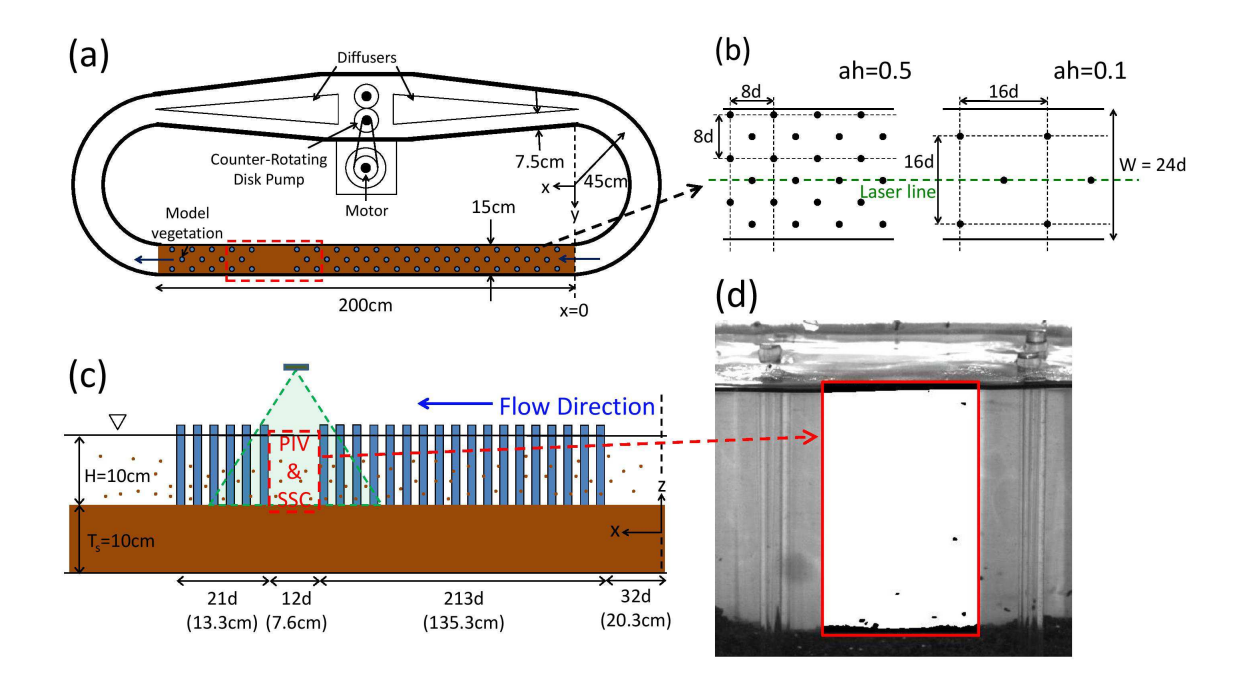


Figure 1. (a) Top-view and (c) side-view sketch of the flume setup and the vegetation array (not to scale), where the water depth, $H=10\ cm$, the thickness of the sediment bed, $T_s=10\ cm$, and the stem diameter, $d=0.64\ cm$. The red-dashed rectangular area indicates the observation region for PIV and SSC measurement. (b) The configuration of the dense (ah=0.5) and the sparse (ah=0.1) vegetation array. The solid dots are the locations of the cylinders. (d) Image processing for identifying sediment particles. The red box indicates the analysis window in the gap. In the window, pixel intensities have been converted into binary values. Black dots indicate the sediment particles with binary value 1, compared to the white background of ambient water with binary value 0.

To account for scaling of sediment dynamics in laboratory experiments (Heller, 2011; Kleinhans et al., 2014), crushed walnut shells are chosen as sediment substrate (Briskin et al., 2002), with a 10 cm thick sediment bed as the initial setup in the straight test region. The sediment density is $\rho_s = 1.2 \ g/cm^3$ (water density, $\rho = 1.0 \ g/cm^3$) with a diameter range 0.84 to 1.68 mm (median grain size, $D_s \approx 1 \ mm$). The walnut shell settling velocity is $w_s \approx 1 \ cm/s$, which is approximated by Rubey (1933)

$$w_s = \left[\sqrt{\frac{2}{3} + \frac{36\nu^2}{(\rho_s/\rho - 1)gD_s^3}} - \sqrt{\frac{36\nu^2}{(\rho_s/\rho - 1)gD_s^3}} \right] \sqrt{(\rho_s/\rho - 1)gD_s^3}$$
 (11)

To ensure sediment resuspension in our tests, mean flow velocities ranged from $1.7 \ cm/s$ to $6 \ cm/s$ within the vegetation canopy $(f=20 \ \text{to} \ 40 \ Hz)$. This range exceeds the estimated critical velocities $(U_c \approx 1.7 \ cm/s \ \text{and} \ 1.5 \ cm/s \ \text{under sparse} \ (ah=0.1)$ and dense (ah=0.5) array with the light-weight sediment, respectively). Critical velocities were estimated by first obtaining the critical velocity under bare-bed condition by Ikeda (1982):

$$\tau_c^* = \frac{u_b^{*2}}{RqD_s} = \frac{4}{3} \frac{\mu}{C_D + \mu C_L} \frac{1}{F^2}$$
 (12)

where $C_L = 0.85C_D$, $F = f(U_0)$, and then updating the values for the vegetated flows based on Yang et al. (2016):

$$U_c = U_0 \frac{1}{\sqrt{1 + B\phi^{2/3}}} \tag{13}$$

where U_c is the critical velocity in vegetated flows, U_0 is the critical velocity under barebed condition, ϕ is the solid volume fraction of the canopy ($\approx (\pi/4)ad$ for circular cylinders), B is the coefficient noted as C in Yang et al. (2016).

Five experimental runs with emergent vegetation arrays and three test runs with bare-bed setup were conducted (Table 1). Under the same f, the mean flow velocity was much higher in the bare-bed cases because of the extra drag exerted by the vegetation. However, the turbulence generated by the vegetation enhanced resuspension, which made the number of suspended particles with vegetation at low speeds similar to the bare-bed case at high speeds. Maximum velocities were capped to ensure adequate capture of individual suspended sediment particles with our quantitative imaging system (details in Section 3.3).

Table 1. Experimental parameters: roughness density, ah, inverter frequency, f, time-averaged mean flow velocity, U, stem Reynolds number, $Re_d = (Ud)/\nu$, near-bed SSC, C_b , image spatial calibration factor, CF (from pixel to cm), and size of three passes used in PIVlab analysis (details in Section 3.2).

Case	ah	$f \\ (Hz)$	$U \ (cm/s)$	Re_d	$C_b \ (g/L)$	CF $(cm/pixel)$	$1^{st}, 2^{nd}, 3^{rd} pass size$ $(pixels)$
1	0.0	20	16.8		2.04	0.0067	64, 32, 16
2	0.0	30	22.0		2.33	0.0067	128, 64, 32
3	0.0	40	30.6		2.44	0.0067	128, 64, 32
4	0.1	20	4.17	265	1.21	0.0071	64, 32, 16
5	0.1	30	6.04	384	1.70	0.0071	128, 64, 32
6	0.5	20	1.76	112	0.78	0.006	64, 32, 16
7	0.5	30	4.66	296	1.15	0.006	64, 32, 16
8	0.5	40	4.94	314	1.32	0.006	128, 64, 32

3.2 Hydrodynamics Measurements

A 5 W continuous-wave laser system was used to generate a vertical planar light sheet for PIV measurement with a thickness of $< 1 \ mm$ at the centerline of the flume. The same setup was used to generate a horizontal light sheet 2 cm below the surface to investigate the horizontal flow structure and validate the 2D vertical-plane approach of the study in our thin flume, where wall effects can be ignored, even for the sparse and bare-bed cases (see details in the supporting information). The light sheet covers the whole observation gap (12 d long) (red-dashed box in Figure 1 (c)). This gap was left to avoid laser reflection issues by the acrylic cylinders within the array. As shown in the supporting information (Fig. S1), velocity measured within the gap is representative of velocity within the array. A 5-Megapixel CCD camera, JAI GO-5000M-USB3, with a Navitar 25 mm focal length was used to capture 8 - bit grayscale images at 60 Hz for 1 minute (3600 images) in each run. Raw images were processed in PIVlab (Thielicke & Stamhuis, 2014). The image spatial calibration factor, CF, for each case is shown in Table 1. Three consecutive 50% size passes with 50% overlapped interrogation areas were used to obtain higher resolution results during cross correlation calculations. The subwindow size

of the first pass followed the one quarter rule (Keane & Adrian, 1990) (detailed size information in Table 1).

3.3 SSC Measurements

SSC was estimated by counting the time-averaged particle pixels in the red-dashed observation area in Figure 1 (c), to quantify the probability of sediment particles to be present at each location. We used bright lighting with white background to contrast particles (dark pixels) and ambient water (white pixels, Figure 1 (d)). Using the same camera as for PIV, 150 images were taken at 0.5 Hz frame rate for each case. We set a threshold intensity to identify sediment particles. We specify a binary value to each pixel (1 = sediment, 0 = water), and average over all frames and along the x-direction to get a time-averaged SSC profile, C(z), as a probability of the presence of sediment grains in the water column. The bed location, z = 0, is determined by the top location where C(z) = 100 %. Calibration for SSC was done by adding known amount of sediments into a small tank with known volume of water, continuously stirred to ensure that sediment particles are well-mixed and uniformly distributed. Following the same method (intensity threshold, binary images, temporal and spatial averaging) with a 5-minute-long record for each known concentration. The near-bed concentration, C_b , for each case is provided in Table 1.

The quantitative imaging method for SSC works well in our thin flume. Sediment grain size was larger than the image pixel size to avoid overestimation of the measured SSC. The amount of suspended sediment particles was limited to an appropriate range to avoid saturation, which would cause extremely dense clouds of suspended sediment that would prevent us from getting an accurate metric. In low speed cases, when there are not many suspended particles, the camera resolution and the size of sediment particles determine a lower-limit baseline, which occurs at some specific z-locations where just a few grains appear on a small number of frames. This is more noticeable in the upper water column near the free surface.

To improve the analysis at low SSC (i.e., low number of recorded particles), a moving-average-frame technique was applied to include the adjacent concentration data into the analysis. The size of the moving frame was designed as 3 to 5 times the sediment size to ensure that the averaging SSC data at each z-location included the entire sediment particle, and averaged over the adjacent region within twice the particle size. More details are described in the supporting information.

4 Results and Discussions

4.1 SSC Profiles of Bare-Bed Channels

To validate the SSC observation method, three bare-bed test cases under different mean flow velocities were conducted and compared with the classical Rouse profile (Equation 4) as shown in Figure 2. The near-bed reference location for the Rouse profile was set as $b=D_s\approx 1$ mm. When the flow velocity goes higher, more sediments are suspended, which makes higher SSC in the water column, showing better agreement between the experimental data and the fitted Rouse profile as R^2 value is as high as 0.86 (Figure 2 (c)). Under lower flow velocity, there are fewer sediments suspended in the water column, resulting in lower SSC profile and larger deviations from the fitted Rouse profile as R^2 value drops to 0.65 (Figure 2 (a)). The deviation, due to the camera resolution and the particle size, is discussed in Section 3.3. However, the fitting coefficient still shows a satisfactory fit, ensuring $R^2>0.65$ among all the cases. In Figure 2 (d), based on the SSC-fitted bed shear velocity, u_b^* , and the mean flow velocity profiles obtained from PIV, the experiment shows consistency with the theoretical log-law profiles in openchannel flows. In Figure 2 (e), u_b^* calculated directly by the near-bed Reynolds stress $\sqrt{-\overline{u'w'}}$

from PIV also matches well with the SSC-fitted u_b^* and the log-law. Those results again validated the current SSC measurement method against the Rouse framework for barebed channels.

282

283

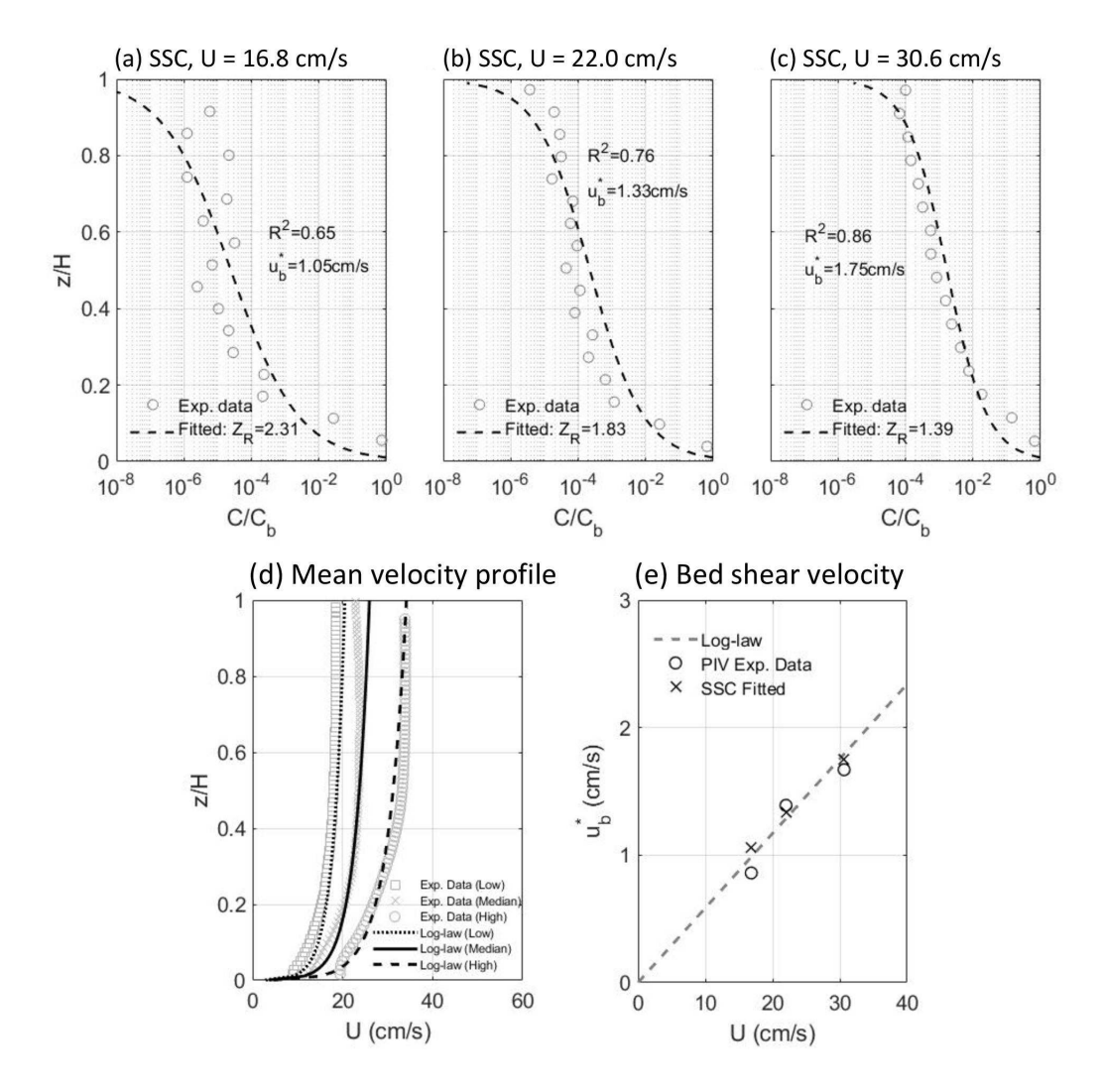


Figure 2. The measured SSC profiles in bare-bed cases under (a) $U=16.8\ cm/s$, (b) $U=22.0\ cm/s$, and (c) $U=30.6\ cm/s$. Grey circles represent experimental data. Black dashed lines represent the fitted profiles of SSC. Comparison of (d) mean velocity profile and (e) bed shear velocity. In (d), grey squares represent experimental data under low flow velocity ($U=16.8\ cm/s$). Grey crosses represent experimental data under medium flow velocity ($U=22.0\ cm/s$). Grey circles represent experimental data under high flow velocity ($U=30.6\ cm/s$). In (e), black circles represent the bed shear velocity calculated with the nearbed Reynolds stress $\sqrt{-u'w'}$ from PIV data. Black crosses represent the fitted bed shear velocity from the measured SSC profiles. The grey dashed line represents the bed shear velocity from the theoretical logarithmic profile in open-channel flows.

4.2 SSC Profiles of Emergent Vegetated Channels

By applying the proposed two-layer model derived in Section 2, Figure 3 shows the model fitted results against the measured SSC data points within emergent arrays. Like the bare-bed case, the near-bed reference location for the model is also set as $b=D_s\approx 1$ mm. The height of the boundary layer region is defined by the vertical location where mean velocity profile reaches a constant value as shown by the dotted line in Figure 3. Within the boundary layer region, flow structure is strongly affected by the flow interaction between bed shear and vegetation stems. The near-bed velocity bulge is one of the features caused by flow coherent structures (e.g., horseshoe vortex and junction vortex), which entrains fast moving fluid with high momentum from the surrounding region into the wake (D. Liu et al., 2008; Stoesser et al., 2010). As a consequence, the varying velocity profile in this region alters SSC, while above H_b , the unchanged mean flow velocity makes a constant SSC profile. The model performs well to predict SSC throughout the entire water column with emergent vegetation. However, the result shows that two critical variables, H_b and u_{beff}^* , change with mean velocity and array density, such that their parameterization is needed for accurate predictions.

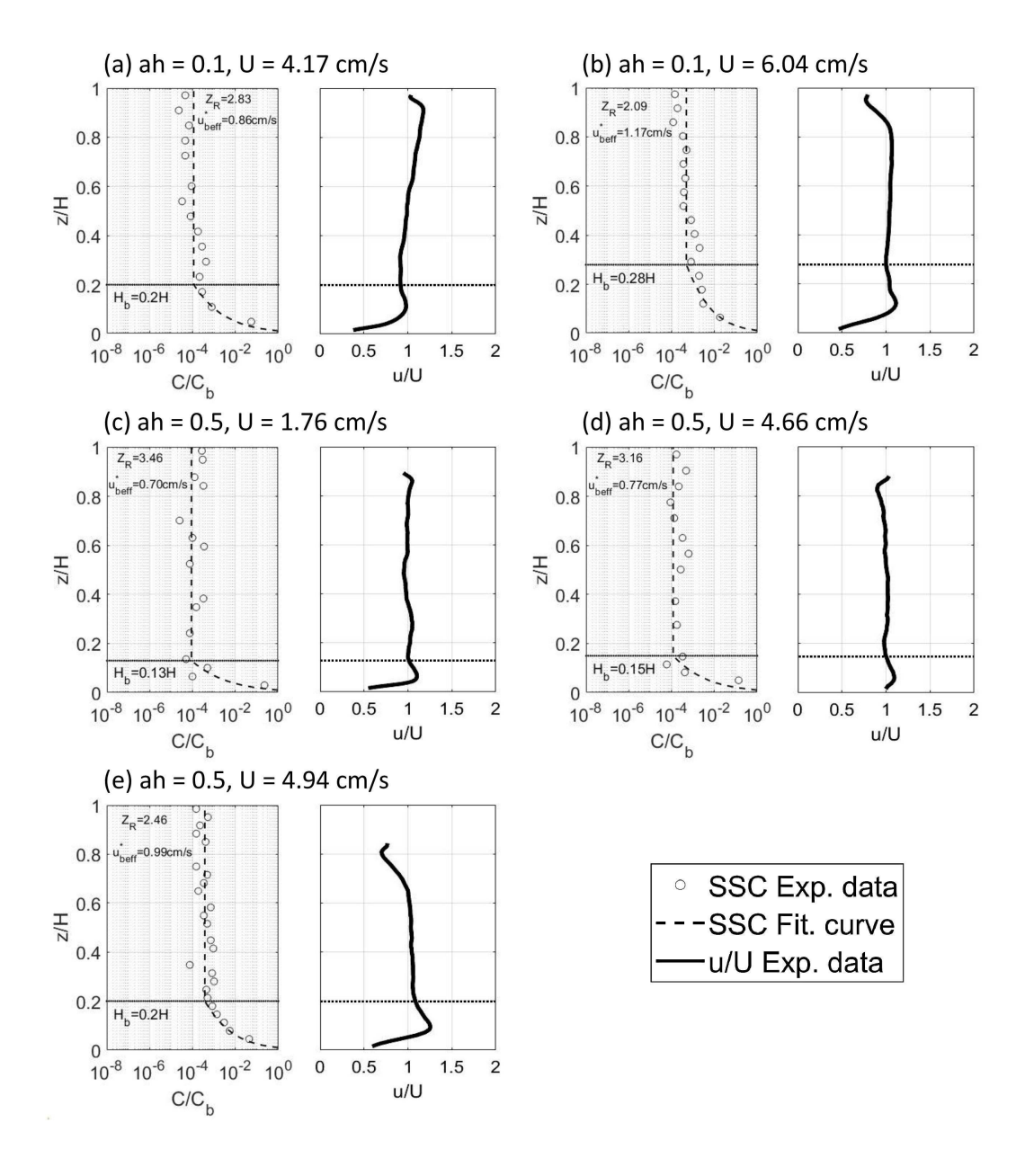


Figure 3. Measured SSC profiles and the corresponding mean velocity profile in flows with emergent vegetation under (a) ah=0.1, $U=4.17\ cm/s$, (b) ah=0.1, $U=6.04\ cm/s$, (c) ah=0.5, $U=1.76\ cm/s$, (d) ah=0.5, $U=4.66\ cm/s$, (e) ah=0.5, $U=4.94\ cm/s$. Grey circles represent experimental data. Black dashed lines represent the fitted curve for SSC profile. Black solid lines represent the velocity profile. Black dotted lines indicate the thickness height of the bottom boundary layer.

4.3 A Model to Predict Thickness Height of the Effective Bottom Boundary Layer

According to previous studies, within the effective bottom boundary layer, the layer thickness height, H_b , is governed by an equilibrium between rates of turbulence production, P, and the viscous dissipation, ϵ , (Brouwers, 2007; Karimpour & Venayagamoor-

301

302

303

304

thy, 2013) $0 \approx P - \epsilon \tag{14}$

Following a similar argument proposed by Etminan et al. (2018) that TKE production in the cylinder wakes balances the rate of work done by form drag (Tanino & Nepf, 2008), turbulence production, P, can thus be expressed as the wake production, P_w , generated by the vegetation. Equation 14 then becomes

$$P_w \approx \epsilon$$
 (15)

 P_w can be further scaled as (Nepf, 1999; Nepf & Vivoni, 2000)

$$P_w \sim \frac{1}{2} C_D a u_b^{*3} \tag{16}$$

where C_D is the drag coefficient of the vegetation canopy, and ϵ can be scaled as

$$\epsilon \sim \frac{\nu u_b^{*2}}{H_b^2} \tag{17}$$

Replacing Equation 16 and 17 back into Equation 15, we obtain

$$H_b^2 \approx \frac{1}{C_D} \frac{2\nu}{au_b^*} \tag{18}$$

In our case, since the roughness density of the canopy is in a range of ah = 0.1 to 0.5, $C_D \approx 1$ can be a valid approximation (Nepf, 1999). Etminan et al. (2018) followed the linear stress model by Yang et al. (2015) to propose an approximation of the bed shear velocity

$$u_b^* = U\sqrt{\frac{2}{Re_{H_v}}}\tag{19}$$

based on the thickness height of viscous layer, H_v , where $Re_{H_v} = UH_v/\nu$. Considering the bottom roughness effect, we followed the form of Equation 19 and assumed that u_b^* is inversely proportional to the roughness Reynolds number $Re_k = Uk_s/\nu$

$$u_b^* \propto U \sqrt{\frac{2}{Re_{k_s}}} \tag{20}$$

where k_s is the bottom roughness. The above assumption of the inverse proportion between u_b^* and k_s is only valid when $k_s/H << 1$. k_s is usually estimated from the sediment size ($k_s = D_s \approx 1 \ mm$ in our cases). Finally, replacing Equation 20 into Equation 18, we estimate H_b based on bottom roughness as

$$H_b = \alpha \frac{1}{C_D^{1/2}} \left(\frac{2\nu k_s}{a^2 U} \right)^{1/4} \tag{21}$$

where α is an empirical coefficient that needs to be experimentally determined. The new proposed H_b estimation in Equation 21 accounts for the bottom roughness effect in natural water environments.

Compared to previous laboratory experiments (D. Liu et al., 2008; Dupuis et al., 2016) and field data (Widdows et al., 2008), covering a range of $Re_d = 100$ to 1, 400, d = 0.5 to 1 cm, and $\phi = 0.006$ to 0.25, Figure 4 (a) shows that the proposed model performs well to predict H_b with $R^2 = 0.75$ and the resulting empirical coefficient $\alpha = 1.52$

The model suggests that H_b increases as U or a decrease, meaning that when the flow velocity is low, the effective bottom boundary layer is thicker, similarly to the turbulent boundary layer becoming thicker when Reynolds number is lower. Also, for sparser

vegetation, the flow can behave more like an open-channel flow, with a larger portion of the flow following the logarithmic profile. Higher k_s will also increase H_b because stronger turbulence can be generated from the rougher bed. However, the model is asymptotic to infinity when $a^2UH^4/\nu k_s \to 0$ as shown in Figure 4 (b), requiring a lower limit of this model according to $H_b/H \leq 1$, which yields:

$$\frac{a^2 U H^4}{\nu k_s} \ge \frac{2\alpha^4}{C_D^2} \tag{22}$$

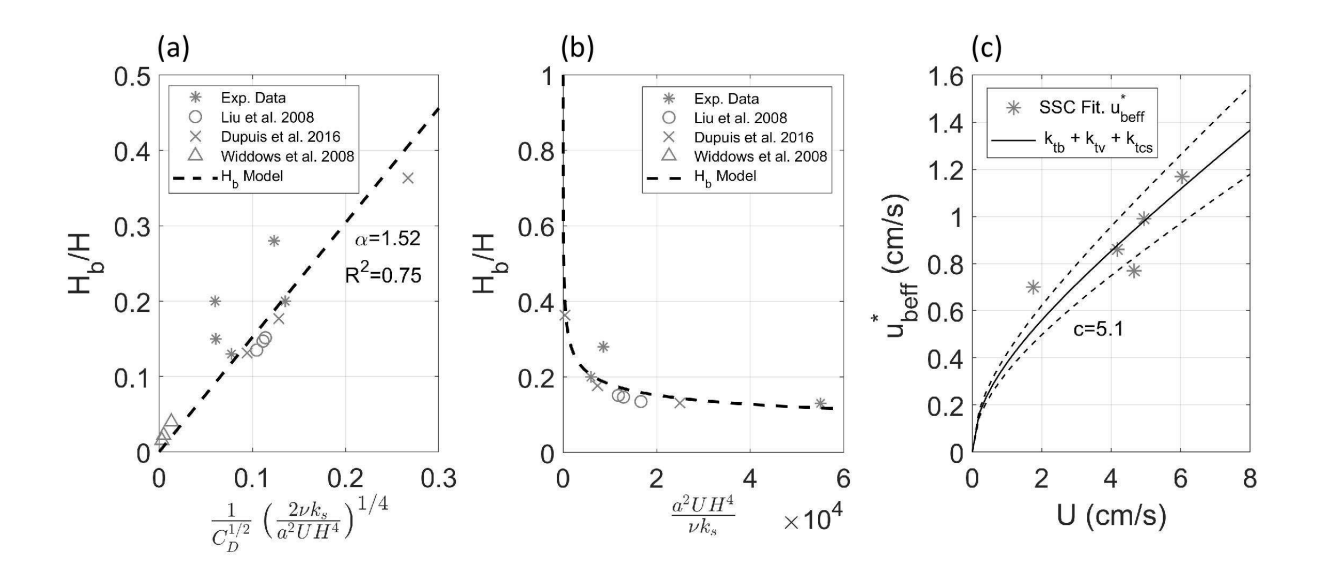


Figure 4. Comparison of the H_b model with (a) the linear fitting result and (b) the zoomed-in region focusing on the lower value region of $a^2UH^4/\nu k_s$. H_b is normalized by the water depth, H. Black dashed line represents the model prediction. Grey stars represent experimental data from the current study. Grey circles represent experimental data from D. Liu et al. (2008). Grey crosses represent experimental data from Dupuis et al. (2016). Grey triangles represent field data from Widdows et al. (2008). The overall model R-squared value is 0.75. (c) Comparison of the modeled and experimental fitted u^*_{beff} against mean flow velocity, U. Grey stars represent experimental data fitted from the SSC profiles in Figure 3. Black solid line represents the mean of the model prediction. Black dashed lines construct a prediction region according to the range of roughness density, ah = 0.1 to 0.5 in the experiment. The model R-squared value is 0.53 to the center black solid line and 0.87 to the dashed region.

4.4 A Turbulence-Based Model to Predict Effective Bed Shear Velocity

Yang and Nepf (2018) showed that sediment incipient motion in vegetated channels depends on the total near-bed TKE, k_t , which is assumed to be the sum of bed-generated turbulence, k_{tb} , and vegetation-generated turbulence, k_{tv} . Then k_{tb} can be approximated by (Stapleton & Huntley, 1995):

$$k_{tb} \approx \frac{u_b^{*2}}{0.19} = \frac{1}{0.19C_{ub}^2}U^2$$
 (23)

where C_{ub} is the integral coefficient that converts mean flow velocity to bed shear velocity based on log-law (Wilcock, 1996)

$$C_{ub} = \frac{U}{u_b^*} = \frac{1}{H} \int_0^H \frac{1}{\kappa} ln\left(30\frac{z}{k_s}\right) dz = \frac{1}{\kappa} \left[ln\left(30\frac{H}{k_s}\right) - 1 \right]$$
 (24)

 k_{tv} can be estimated by (Tanino & Nepf, 2008)

$$k_{tv} = 1.2 \left[C_D \frac{\phi}{(1-\phi)\pi/2} \right]^{2/3} U^2$$
 (25)

The above k_{tv} estimation is valid when $Re_d > 120$ (C. Liu & Nepf, 2016) and d/s < 0.56 (Tanino & Nepf, 2008), which works for the current experimental setup.

However, to predict the mean SSC profile, local fluxes of sediment entrainment by near-bed coherent structures should also be considered. Hence, k_t can be modified as

$$k_t = k_{tb} + k_{tv} + k_{tcs} \tag{26}$$

where k_{tcs} is the TKE component by the near-bed coherent structures. Since the loglaw is assumed valid in the effective bottom boundary layer, we can follow the same approximation for k_{tb} to estimate the effective bed shear velocity, u_{beff}^* , based on Equation 26

$$u_{beff}^* \approx \sqrt{0.19(k_{tb} + k_{tv} + k_{tcs})}$$
 (27)

Okayasu et al. (2010) proposed a modified effective bed shear stress equation by adding a component that is proportional to the root-mean-square (rms) value of the mean bed shear stress, τ_b^{rms}

$$\tau_b = \overline{\tau_b} + c\tau_b^{rms} \tag{28}$$

where τ_b is the effective bed shear stress, $\overline{\tau_b}$ is the mean bed shear stress, c is an empirical coefficient which depends on the shape, orientation, array density, and stem Reynolds number, Re_d . Then, k_{tcs} can be approximated from τ_b^{rms} in a similar way as k_{tb}

$$k_{tcs} \approx \frac{c}{0.19} u_{rms}^{*2} \tag{29}$$

where $u_{rms}^*{}^2 = \tau_b^{rms}/\rho$. Chang et al. (2017) provided a scaling method to estimate u_{rms}^*

$$u_{rms}^* = U \left(\frac{1}{Re} \frac{\sqrt{k_{t0}}/U}{z_0/H} \right)^{1/2}$$
 (30)

where z_0 is a near-bed reference vertical location, k_{t0} is the TKE at $z=z_0$. In our case, we set $z_0=k_s$, $k_{t0}=k_{tb}+k_{tv}$, $Re=(UH/\nu)$, then Equation 30 becomes

$$u_{rms}^* = \left(\frac{\nu}{k_s} \sqrt{k_{tb} + k_{tv}}\right)^{1/2} \tag{31}$$

Replacing Equation 31 and 29 back into Equation 27, we can finally obtain the estimated u_{beff}^* :

$$u_{b\,eff}^* \approx \sqrt{0.19(k_{tb} + k_{tv} + \frac{c}{0.19} \frac{\nu}{k_s} \sqrt{k_{tb} + k_{tv}})}$$
 (32)

where k_{tb} and k_{tv} can be estimated by Equation 23 and Equation 25, respectively.

Figure 4 (c) shows the comparison of the modeled and experimental fitted u_{beff}^* . Two dashed lines provide a predicting region according to the range of ah=01 to 0.5 in the experiment. The model makes a prediction of u_{beff}^* with $R^2=0.53$ to the center black solid line and $R^2=0.87$ to the dashed region. The best fitted empirical coefficient, c=5.1, which is close to the suggested c=4.1 for circular cylinders by previous numerical study using Detached Eddy Simulations (DES) (Cheng et al., 2018). However, as mentioned, the empirical value, c, varies under different Re_d and ah. High SSC

values can potentially cause turbulence modulation in the flow. However, the ranges of SSC observed in our study are low enough to avoid such particle feedbacks and potential turbulence stratification effects (Cao et al., 2003). High SSC and a sharp SSC gradient only occur in the near-bed region, which could introduce particle feedbacks to influence the magnitude of c. To obtain a more comprehensive range of c would require more experimental or numerical studies, considering a broad range of sediment size, density, and vegetation characteristics, which is out of the scope of the current study.

4.5 Model Application

397

401

402

403

404

406

407

408

410

411

412

413

414

415

416

417

418

421

422

423

425

426

429

430

431

432

433

434

435

437

439

440

441

According to the proposed two-layer model and the associated turbulence-based parameterizations of H_b and $u_{b\,eff}^*$, we can predict SSC in flows with emergent vegetation by following the procedure summarized as follows:

- Use Equation 21 to estimate the thickness height of the effective bottom boundary layer, H_b , based on the measured mean flow velocity, U, and the frontal area of vegetation canopy, a, within the limitation range shown by Equation 22.
- Use Equation 32 to estimate the effective bed shear velocity, u_{beff}^* , which considers turbulence generated from the vegetation, the bed, and the coherent structures caused by stem-bed-flow interaction.
- Use the estimated H_b and u_{beff}^* from the previous steps into Equation 10. Use the measured C_b and the known $b \ (= k_s = D_s)$ and w_s from the sediment properties to predict SSC profiles.

5 Conclusions

The vegetation-generated turbulence alters the flow structure and interacts with bed-generated turbulence, creating near-bed coherent structures that enhance sediment suspension. The traditional Rouse profile derived from the classic parabolic profile of ν_t in open-channel flows fails to accurately predict SSC in regions with aquatic vegetation. We propose a two-layer model based on mean flow and turbulent stress profiles with two additional turbulence-based models that provide estimations of the effective bottom boundary layer thickness, H_b , and the effective bed shear velocity u_{beff}^* . The models show that H_b increases as U or a decrease, while u_{beff}^* is determined by a combination of k_{tv} and k_{tb} with an empirical constant, c, to parameterize the local fluxes of sediment entrainment by near-bed coherent structures. More experimental or numerical studies are needed to obtain a more comprehensive expression of c, which varies under different Re_d and ah. Experimental results and observations from previous studies validated the newly developed two-layer model under $ah = \{0.1 - 0.5\}$ and $Re_d = \{100 - 400\}$, which provides better prediction and more detailed insights on sediment resuspension and SSC in emergent vegetated flows. The model is expected to deliver critical information for future studies on landscape evolution and water quality management in vegetated channels, wetlands, and estuaries.

Acknowledgments

CT acknowledges funding support from Taiwan-UIUC Fellowship. This study was supported by NSF through CAREER EAR 1753200. Any Opinions, findings and conclusions or recommendations expressed in this material are those of the authors and do not necessarily reflect those of the National Science Foundation. The authors are grateful to the editor and two anonymous reviewers for their thoughtful and constructive comments on improving and clarifying the article. Data presented in this article is available through Figshare data repository (doi.org/10.6084/m9.figshare.13333769).

References

- Apsilidis, N., Diplas, P., Dancey, C. L., & Bouratsis, P. (2015). Time-resolved flow dynamics and reynolds number effects at a wallcylinder junction. *Journal of Fluid Mechanics*, 776, 475-511.
 - Bouillon, S., Borges, A. V., CastanedaMoya, E., Diele, K., Dittmar, T., Duke, N. C., ... Twilley, R. R. (2008). Mangrove production and carbon sinks: a revision of global budget estimates. *Global Biogeochemical Cycles*, 22(2), 1-12.
 - Briskin, B. J., Cantero, M. I., & Garcia, M. H. (2002). In-situ measurements of sediment oxygen demand by suspended biosolids. *Hydraulic Measurements and Experimental Methods*, 1-10.
 - Brouwers, J. J. H. (2007). Dissipation equals production in the log layer of wall-induced turbulence. *Physics of Fluids*, 19(10), 101702.
 - Cao, Z., Egashira, S., & Carling, P. A. (2003). Role of suspendedsediment particle size in modifying velocity profiles in open channel flows. Water Resources Research, 39(2), 1-15.
 - Chang, W. Y., Constantinescu, G., & Tsai, W. F. (2017). On the flow and coherent structures generated by a circular array of rigid emerged cylinders placed in an open channel with flat and deformed bed. *Journal of Fluid Mechanics*, 831, 1-40.
 - Cheng, Z., Koken, M., & Constantinescu, G. (2018). Approximate methodology to account for effects of coherent structures on sediment entrainment in rans simulations with a movable bed and applications to pier scour. Advances in Water Resources, 120, 65-82.
 - Dalrymple, R. W., & Choi, K. (2007). Morphologic and facies trends through the fluvialmarine transition in tide-dominated depositional systems: a schematic framework for environmental and sequence-stratigraphic interpretation. *Earth-Science Reviews*, 81(3-4), 135174.
 - Danielsen, F., Sorensen, M. K., Olwig, M. F., Selvam, V., Parish, F., Burgess, N. D., ... Suryadiputra, N. (2005). The asian tsunami: A protective role for coastal vegetation. *Science*, 310(5748), 643.
 - Defina, A., & Bixio, A. C. (2005). Mean flow and turbulence in vegetated open channel flow. Water Resources Research, 41(7), 1-12.
 - Diplas, P., Dancey, C. L., Celik, A. O., Valyrakis, M., Greer, K., & Akar, T. (2008). The role of impulse on the initiation of particle movement under turbulent flow conditions. *Science*, 322(5902), 717-720.
 - Duarte, C. M., Marba, N., Garcia, E., Fourqurean, J. W., Beggins, J., Barron, C., & Apostolaki, E. T. (2010). Seagrass community metabolism: Assessing the carbon sink capacity of seagrass meadows. Global Biogeochemical Cycles, 24(4), 1-8.
 - Dupuis, V., Proust, S., Berni, C., & Paquier, A. (2016). Combined effects of bed friction and emergent cylinder drag in open channel flow. *Environmental Fluid Mechanics*, 16(6), 1173-1193.
 - Engelund, F., & Fredsoe, J. (1976). A sediment transport model for straight alluvial channels. *Nordic Hydrology*, 7, 293306.
 - Etminan, V., Ghisalberti, M., & Lowe, R. J. (2018). Predicting bed shear stresses in vegetated channels. *Water Resources Research*, 54(11), 9187-9206.
 - Garcia, M. (2008). Sedimentation engineering: processes, measurements, modeling, and practice. *American Society of Civil Engineers*.
 - Hanmaiahgari, P. R., Roussinova, V., & Balachandar, R. (2017). Turbulence characteristics of flow in an open channel with temporally varying mobile bedforms. Journal of Hydrology and Hydromechanics, 65(1), 35-48.
- Heller, V. (2011). Scale effects in physical hydraulic engineering models. *Journal of Hydraulic Research*, 49(3), 293-306.
- Ikeda, S. (1982). Incipient motion of sand particles on side slopes. journal of the hydraulics division. *Journal of the Hydraulics Division*, 108(1), 95-114.

Kakeh, N., Coco, G., & Marani, M. (2015). On the morphodynamic stability of intertidal environments and the role of vegetation. Advances in Water Resources, 93, 303-314.

- Karimpour, F., & Venayagamoorthy, S. K. (2013). Some insights for the prediction of near-wall turbulence. *Journal of Fluid Mechanics*, 723, 126-139.
- Keane, R. D., & Adrian, R. J. (1990). Optimization of particle image velocimeters. i. double pulsed systems. *Measurement Science and Technology*, 1(11), 1202.
- Kennedy, H., Beggins, J., Duarte, C. M., Fourqurean, J. W., Holmer, M., Marba, N., & Middelburg, J. J. (2010). Seagrass sediments as a global carbon sink: Isotopic constraints. *Global Biogeochemical Cycles*, 24(4), 1-8.
- Kleinhans, M. G., van Dijk, W. M., van de Lageweg, W. I., Hoyal, D. C. J. D., Markies, H., van Maarseveen, M., . . . Cheshier, N. (2014). Quantifiable effectiveness of experimental scaling of river- and delta morphodynamics and stratigraphy. *Earth-Science Reviews*, 133, 43-61.
- Li, J., Qi, M., Fuhrman, D. R., & Chen, Q. (2018). Influence of turbulent horse-shoe vortex and associated bed shear stress on sediment transport in front of a cylinder. *Experimental Thermal and Fluid Science*, 97, 444-457.
- Liu, C., & Nepf, H. (2016). Sediment deposition within and around a finite patch of model vegetation over a range of channel velocity. Water Resources Research, 52(1), 600-612.
- Liu, D., Diplas, P., Fairbanks, J. D., & Hodges, C. C. (2008). An experimental study of flow through rigid vegetation. *Journal of Geophysical Research: Earth Surface*, 113(F4), 1-16.
- Lopez, F., & Garcia, M. (1998). Openchannel flow through simulated vegetation: Suspended sediment transport modeling. Water resources research, 34(9), 2341-2352.
- Marani, M., D'Alpaos, A., Lanzoni, S., & Santalucia, M. (2011). Understanding and predicting wave erosion of marsh edges. *Geophysical Research Letters*, 38(21), 1-5.
- Mcleod, E., Chmura, G., Bouillon, S., Salm, R., Bjork, M., Duarte, C. M., ... Silliman, B. R. (2011). A blueprint for blue carbon: toward an improved understanding of the role of vegetated coastal habitats in sequestering co_2 . Frontiers in Ecology and the Environment, 9(10), 552-560.
- Meyer-Peter, E., & Muller, R. (1948). Formulas for bed-load transport. *Proceedings* of the 2nd Congress, IAHR, Stockholm, 39-64.
- Micheli, E., & Kirchner, J. (2002). Effects of wet meadow riparian vegetation on streambank erosion: 2. measurements of vegetated bank strength and consequences for failure mechanics. Earth Surface Processes and Landforms, 27(7), 687-697.
- Nepf, H. M. (1999). Drag, turbulence, and diffusion in flow through emergent vegetation. Water Resource Research, 35(2), 479-489.
- Nepf, H. M. (2012). Flow and transport in regions with aquatic vegetation. *Annual Review of Fluid Mechanics*, 44, 123-142.
- Nepf, H. M., & Vivoni, E. R. (2000). Flow structure in depth-limited, vegetated flow. *Journal of Geophysical Research: Oceans*, 105(C12), 28547-28557.
- Nino, Y., & Garcia, M. H. (1996). Experiments on particleturbulence interactions in the nearwall region of an open channel flow: Implications for sediment transport. *Journal of Fluid Mechanics*, 326, 285-319.
 - Nino, Y., & Garcia, M. H. (1998). Using lagrangian particle saltation observations for bedload sediment transport modeling. *Hydrological Processes*, 12, 1197-1218.
- O'Connor, B. L., & Hondzo, M. (2008). Dissolved oxygen transfer to sediments by sweep and eject motions in aquatic environments. *Limnology and Oceanogra*phy, 53(2), 566-578.

Odell, G. M., & Kovasznay, L. S. (1971). A new type of water channel with density stratification. *Journal of Fluid Mechanics*, 50(3), 535-543.

- Okayasu, A., Fujii, K., & Isobe, M. (2010). Effect of external turbulence on sediment pickup rate. *Proceedings of the 32nd International Conference on Coastal Engineering*.
- Paola, C., Twilley, R. R., Edmonds, D. A., Kim, W., Mohrig, D., Parker, G., ... Voller, V. R. (2011). Natural processes in delta restoration: Application to the mississippi delta. *Annual Review of Marine Science*, 3, 67-91.
 - Parker, G. (1979). Hydraulic geometry of active gravel rivers. *Journal of Hydraulic Engineering*, 105(9), 1185-1201.
 - Raupach, M. R., & Thom, A. S. (1981). Turbulence in and above plant canopies. Annual Review of Fluid Mechanics, 13, 97-129.
 - Rouse, H. (1937). Modern conceptions of the mechanics of fluid turbulence. *Trans* ASCE, 102, 463-505.
 - Rubey, W. W. (1933). Settling velocity of gravel, sand, and silt particles. *American Journal of Science*, 25(148), 325338.
 - Schanderl, W., Jenssen, U., & Manhart, M. (2017). Near-wall stress balance in front of a wall-mounted cylinder. Flow, Turbulence and Combustion, 99(3-4), 665-684.
 - Schanderl, W., Jenssen, U., Strobl, C., & Manhart, M. (2017). The structure and budget of turbulent kinetic energy in front of a wall-mounted cylinder. *Journal of Fluid Mechanics*, 827, 285-321.
 - Schultz, M. P., & Flack, K. A. (2007). The rough-wall turbulent boundary layer from the hydraulically smooth to the fully rough regime. *Journal of Fluid Mechanics*, 580, 381.
 - Shaw, R. H. (1977). Secondary wind speed maxima inside plant canopies. *Journal of Applied Meteorology*, 16(5), 514-521.
 - Stapleton, K. R., & Huntley, D. A. (1995). Seabed stress determinations using the inertial dissipation method and the turbulent kinetic energy method. *Earth Surface Processes and Landforms*, 20(9), 807-815.
 - Stoesser, T., Kim, S. J., & Diplas, P. (2010). Turbulent flow through idealized emergent vegetation. *Journal of Hydraulic Engineering*, 136(12), 1003-1017.
 - Sumer, B. M., Chua, L. H., Cheng, N.-S., & Fredsoe, J. (2003). Influence of turbulence on bed load sediment transport. *Journal of Hydraulic Engineering*, 129(8), 585-596.
 - Syvitski, J. P., Kettner, A. J., Overeem, I., Hutton, E. W., Hannon, M. T., Brakenridge, G. R., . . . Nicholls, R. J. (2009). Sinking deltas due to human activities. *Nature Geoscience*, 2(10), 681-686.
 - Tanino, Y., & Nepf, H. M. (2008). Lateral dispersion in random cylinder arrays at high reynolds number. *Journal of Fluid Mechanics*, 600, 339-371.
 - Thielicke, W., & Stamhuis, E. J. (2014). Pivlab-towards user-friendly, affordable and accurate digital particle image velocimetry in matlab. *Journal of Open Research Software*, 2, 1-10.
 - Tinoco, R. O., & Coco, G. (2014). Observations of the effect of emergent vegetation on sediment resuspension under unidirectional currents and waves. *Earth Surface Dynamics*, 2(1), 83-96.
 - Tinoco, R. O., & Coco, G. (2016). A laboratory study on sediment resuspension within arrays of rigid cylinders. Advances in Water Resources, 92, 1-9.
 - van Rijn, L. C. (1984). Sediment pick-up functions. *Journal of Hydraulic Engineering*, 110(10), 14941503.
 - Waterman, D. M., Liu, X., Motta, D., & Garcia, M. H. (2016). Analytical lagrangian model of sediment oxygen demand and reaeration flux coevolution in streams. *Journal of Environmental Engineering*, 142(7), 04016028.
- Weston, N. B. (2014). Declining sediments and rising seas: An unfortunate convergence for tidal wetlands. *Estuaries and Coasts*, 37(1), 1-23.

Widdows, J., Pope, N. D., & Brinsley, M. D. (2008). Effect of spartina anglica stems
 on near-bed hydrodynamics, sediment erodability and morphological changes
 on an intertidal mudflat. Marine Ecology Progress Series, 362, 45-57.

610

611

612

613

614

615

617

618

619

620

622

- Wilcock, P. R. (1996). Estimating local bed shear stress from velocity observations. Water Resources Research, 32(11), 3361-3366.
- Yager, E. M., & Schmeeckle, M. W. (2013). The influence of vegetation on turbulence and bed load transport. *Journal of Geophysical Research: Earth Surface*, 118(3), 1585-1601.
- Yalin, M. S. (1963). An expression for bed-load transportation. *Journal of the Hydraulic Division*, 89, 221-250.
- Yang, J. Q., Chung, H., & Nepf, H. M. (2016). The onset of sediment transport in vegetated channels predicted by turbulent kinetic energy. *Geophysical Research Letters*, 43(11), 261-268.
- Yang, J. Q., Kerger, F., & Nepf, H. M. (2015). Estimation of the bed shear stress in vegetated and bare channels with smooth beds. Water Resources Research, 51(5), 3641-3663.
 - Yang, J. Q., & Nepf, H. M. (2018). A turbulence-based bed-load transport model for bare and vegetated channels. *Geophysical Research Letters*, 45(10), 428-436.